Reynolds Stress Transport Modeling for Steady and Unsteady Channel Flows with wall injection

Bruno Chaouat*
ONERA , 92322 Châtillon, France

Roland Schiestel**
IRPHE, Château-Gombert, 13384 Marseille, France

Abstract

Predictions of steady and unsteady injection driven flows in a plane channel are performed by solving the averaged Navier-Stokes equations using a compressible Reynolds stress model. The boundary condition for the fluid injection through the porous wall has been formulated by taking into account experimental investigations. Depending of the Reynolds number, the flow can be steady or unsteady. For the steady flow, laminar to turbulent regimes are reproduced in good agreement with the experimental data for both the velocity and the turbulent stresses. For the unsteady flow which result from natural instabilities, the resonant frequency quite close to the second longitudinal acoustic mode as well as the coherent flow structures are fairly well predicted in comparison to experiment. Animations for the vorticity and entropy contours show the mechanism of the vortex shedding which develops in the channel.

1 Introduction

Turbulence plays a significant role in the flow in solid propellant rocket motors (SRM) through its influence on the momentum and energy transfers in the motor chamber. The flow in SRM results from the propellant burning and differs appreciably from a standard duct flow bounded by impermeables walls. For fluid dynamics investigations, the flow in SRM can be modeled by a duct flow with fluid injection through a porous wall. Different duct flow regimes can occur, depending on the injection Reynolds number $R_s = u_s\delta/\nu$ where u_s, δ and ν represent the injection velocity at the permeable surface, the diameter and the kinematic viscosity [1]. The flow can evolve spatially

*Senior Scientist, Department of Computational Fluid Dynamics. E-mail address: Bruno.Chaouat@onera.fr
** Senior Scientist at CNRS.

This article was chosen from Selected Proceedings of the Second International Symposium on Turbulence and Shear Flow Phenomena (KTH-Stockholm, 27-29 June 2001) ed E. Lindborg, A. Johansson, J. Eaton, J. Humphrey, N. Kasagi, M. Leschziner and M. Sommerfeld.

from a laminar to a steady turbulent regime, with a transition process [2]. It can also be oscillating due to the coupling between vortices generated by the hydrodynamic instability mechanism and the chamber acoustic modes [3, 4]. In the case where the vortices are emitted at a frequency close to the one of a longitudinal acoustic mode, the flow is characterized by an acoustic resonant regime. These different flow regimes affect the ballistics predictions of motors. For instance, large solid propellant boosters for space launchers may exhibit low pressure and thrust oscillations. For engineering applications, the knowledge of the flow structure and the acting mechanisms are of major importance for predicting the motor operating conditions. Direct numerical simulation (DNS) of the whole flow domain in a chamber of a solid rocket motor can not be performed because of the size of the chamber. Recently, only a small flow domain in a motor chamber has been simulated by this approach [5]. However, because of the mass injection through the wall, the inlet and outlet boundary conditions of the computational domain are not periodic. So that specific adaptations of the numerical method must be implemented in the code to overcome these difficulties. Large Eddy Simulation (LES) is a promising route for studying motor internal flows. It allows a good description of the turbulence interaction mechanisms. For instance, Silvestrini [6] simulated the flows in a simplified geometry of a porous walled channel with an inclined backward-facing trailing edge using LES model based on a filtered or selective structure function [7]. For that geometry, it has been found that the shear layers of the flow were mainly caused by the injecting surface singular point, as already observed in previous computations [8]. Recently, Apte and Yang [9] performed computation of a plane channel flow with fluid injection through the wall using a dynamic Smagorinsky model. Their simulation succeeded in reproducing the vortex-stretching and rolling mechanisms of the flow. Although that LES has demonstrated his capability to handle such complex flows, it still requires very large computational time despite the recent progess in computers. Therefore, in a more practical way for engineering applications, flows in SRM have been modeled using Reynolds average Navier-Stokes equations (RANS). In the past, several authors made such flow predictions using first order turbulence model such as $k-\epsilon$ or $k-\omega$. However, this model has not given satisfactory flow predictions in SRM. In particular, for steady flows which evolve spatially from laminar to turbulent regime, the transition process and the turbulence levels in the post transition zone could not be reproduced [10, 11, 12]. The flow turbulence levels were overpredicted by about 200% and 300% in the post-transition of the flow. These results show that more advanced turbulent models must be used for SRM applications. Contrary to first order turbulence model, second order turbulence model based on the transport equation of each individual Reynolds stress provides a better description of the flow physics. This is mainly due to the pressure-strain correlation term in the Reynolds stress model (RSM) which plays a pivotal role in determing the structure of turbulent flows. This term of major importance redistributes turbulent energy among the Reynolds stress components. It is composed by a slow and rapid parts which take into account the flow anisotropy. In the past, this term has been modeled by assuming homogeneous flows that are near equilibrium. Then, recent improvements have been made using different approaches. For instance, Speziale has obtained a general form of the redistribution term using tensorial invariance properties [13]. Schiestel has taken into account multiple turbulence scales in the model [14]. For SRM applications, Beddini used an RSM turbulent model in a previous formulation based on transport equations of Reynolds stresses with an algebric relation for the turbulence macro-length scale [15]. A reasonable agreement with experimental data was obtained for a duct flow with wall injection [16].

The present study is concerned with advanced second order turbulence transport modeling of steady and unsteady flows with natural instabilities in planar channel. The aim is to predict accurately the flowfield in a cold flow set up called VECLA which has been developed at ONERA. In this work, the model of Launder and Shima [17] has been selected because it embodies some advanced concepts and contains only a few empirical terms. Thus it is a good candidate to handle a large variety of flows. The original model has been extended for compressible flows and modified for channel flows with effect of spanwise rotation or wall injection through a porous wall [18, 19]. It has predicted turbulence in rotating channel flows in good agreement with LES data [20]. In the present study, we show that this level of closure is able to reproduce both steady and unsteady injection induceed flows with a good description of the acting mechanisms.

2 Experimental setup

The experimental setup VECLA [21] is a plane channel bounded on one side by a porous plate made of sintered bronze and on the other side by an impermeable wall as indicated in figure (1). The size of the porosity of the porous material is 8 μm. Cold air at 303 K is injected with a uniform mass flow rate m. The length of the channel is 581 mm. By adjusting the height of the channel δ and the injection velocity u_s, different flow regimes can be realized. In particular, for $\delta = 10$ mm, $m = 2.619$ kg/m^2s, $u_s \approx 1.36$ m/s, $R_s \approx 1600$, the steady flow undergoes a transition process from the laminar to turbulent regime. For $\delta = 20$ mm, $m = 2.04$ kg/$m^2 s$, $u_s \approx 1.70$ m/s, $R_s \approx 2200$, the flow becomes unsteady and presents an acoustic resonant regime. It is of interest to note that linear stability theory shows that the axial-flow Reynolds number at neutral stability increases linearly for large values of the injection Reynolds number [1]. Velocity measurement have been performed with a hot wire probe located at different cross sections of the channel.

3 Governing equations

Turbulent flow of a viscous fluid is considered. As in the usual treatment of turbulence, the flow variable $\phi = \rho\xi$, where ρ is the mass density, is decomposed into an ensemble average and fluctuating parts as $\phi = \overline{\phi} + \phi'$. In the present case, the Favre average is used for compressible fluid so that the variable ξ can be written as $\xi = \tilde{\xi} + \xi''$ with the particular properties $\tilde{\xi''} = 0$ and $\overline{\rho\xi''} = 0$. These relations imply that $\tilde{\xi} = \overline{\rho\xi}/\bar{\rho}$. The ensemble average of the Navier-Stokes equations produces in Favre variables the following forms of the mass, momentum and energy equations written in a general rotating frame of reference $\mathbf{\Omega}$:

$$\frac{\partial \bar{\rho}}{\partial t} + \frac{\partial}{\partial x_j}\left(\bar{\rho}\tilde{u}_j\right) = 0 \tag{1}$$

$$\frac{\partial}{\partial t}\left(\bar{\rho}\,\tilde{u}_i\right) + \frac{\partial}{\partial x_j}(\bar{\rho}\,\tilde{u}_i\,\tilde{u}_j) = \frac{\partial \bar{\Sigma}_{ij}}{\partial x_j} - 2\epsilon_{ijk}\bar{\rho}\Omega_j\bar{u}_k \tag{2}$$

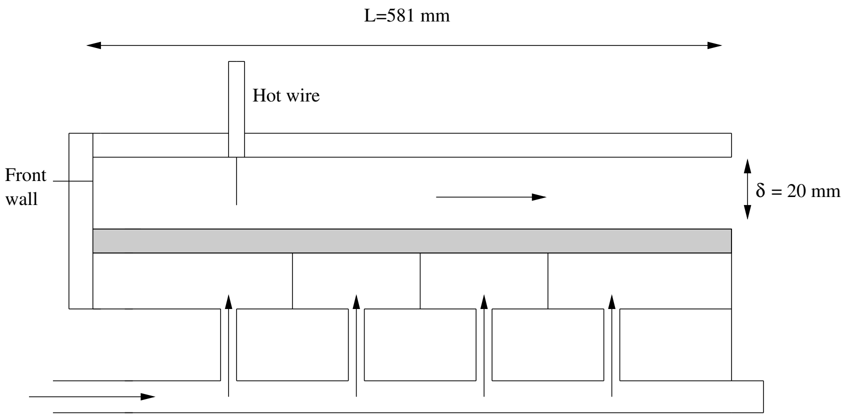

Figure 1: Sketch of VECLA facility

$$\frac{\partial}{\partial t}(\bar{\rho}\,\tilde{E}) + \frac{\partial}{\partial x_j}(\bar{\rho}\,\tilde{E}\,\tilde{u}_j) = \frac{\partial}{\partial x_j}\left(\bar{\Sigma}_{ij}\tilde{u}_i\right)$$
$$+\frac{\partial}{\partial x_j}\left(\overline{\sigma_{ij}u_i''} - \tfrac{1}{2}\bar{\rho}\,\widetilde{u_k''u_k''u_j''}\right) - \frac{\partial \bar{q}_j}{\partial x_j} \tag{3}$$

where u_i, E, Σ_{ij}, σ_{ij}, q_i are the velocity vector, the total energy, the total stress tensor, the viscous stress tensor and the total heat flux vector, respectively. The mean stress tensor $\bar{\Sigma}_{ij}$ is composed by the mean modified pressure $\bar{p^*}$, the mean viscous stress $\bar{\sigma}_{ij}$ and the turbulent stress $\bar{\rho}\,\tau_{ij}$ as follows :

$$\bar{\Sigma}_{ij} = -\bar{p^*}\,\delta_{ij} + \bar{\sigma}_{ij} - \bar{\rho}\,\tau_{ij} \tag{4}$$

where $\bar{p^*} = \bar{p} - \frac{1}{2}\bar{\rho}|\mathbf{\Omega}\times\mathbf{x}|^2$. In the present application, $\mathbf{\Omega} = 0$. In this expression, the tensor $\bar{\sigma}_{ij}$ takes the usual form :

$$\bar{\sigma}_{ij} = 2\bar{\mu}\bar{S}_{ij} - \frac{2}{3}\bar{\mu}\frac{\partial \bar{u}_k}{\partial x_k}\delta_{ij} \tag{5}$$

where the mean strain rate $\bar{S}_{ij}$ and and the Favre-averaged Reynolds stress tensor τ_{ij} are defined respectively by :

$$\bar{S}_{ij} = \frac{1}{2}\left(\frac{\partial \bar{u}_i}{\partial x_j} + \frac{\partial \bar{u}_j}{\partial x_i}\right) \tag{6}$$

$$\tau_{ij} = \widetilde{u_i''u_j''} \tag{7}$$

and μ is the molecular viscosity. Assuming ideal gas law, the mean thermodynamic pressure is computed by:

$$\bar{p} = (\gamma - 1)\bar{\rho}\left(\tilde{E} - \tfrac{1}{2}\tilde{u}_i\tilde{u}_i - \tfrac{1}{2}\tau_{ii}\right) \tag{8}$$

where γ is the ratio of specific heats. The presence of the turbulent contribution τ_{ii} in equation (8) shows a coupling between the mean equations and the turbulent transport equations. The mean heat flux $\bar{q}_i$ is composed of the laminar and turbulent flux contributions:

$$\bar{q}_i = -\bar{\kappa}\frac{\partial \bar{T}}{\partial x_i} + \bar{\rho}\,\widetilde{h'' u''_i} \tag{9}$$

where T, h and κ are, respectively, the temperature, the specific enthalpy and the thermal conductivity. Closure of the mean flow equations is necessary for the turbulent stress $\bar{\rho}\,\widetilde{u''_i u''_j}$ of the total stress tensor Σ_{ij} which appears in the momentum equation (2) and energy equation (3), as well as for the turbulent transport $\overline{\sigma_{ij} u''_i} - \frac{1}{2}\bar{\rho}\,\widetilde{u''_k u''_k u''_j}$ and the turbulent heat flux $\bar{\rho}\,\widetilde{h'' u''_i}$ which are present in the energy equation (3). The Favre-averaged correlation tensor $\tau_{ij} = \widetilde{u''_i u''_j}$ is computed by the Reynolds stress model of Launder and Shima [17] which has been extended for compressible flows, developed for rotation and modified for wall injection [18, 19]. In a general case of rotating frame, the transport equation of the Reynolds stress tensor is:

$$\begin{aligned}\frac{\partial}{\partial t}(\bar{\rho}\,\tau_{ij}) + \frac{\partial}{\partial x_k}(\bar{\rho}\,\tau_{ij}\tilde{u}_k) &= J_{ij} + P_{ij} + P^R_{ij} - \frac{2}{3}\bar{\rho}\epsilon\delta_{ij} \\ &+ \Phi^1_{ij} + \Phi^2_{ij} + \Phi^w_{ij}\end{aligned} \tag{10}$$

where :

$$J_{ij} = \frac{\partial}{\partial x_k}\left(\bar{\mu}\frac{\partial \tau_{ij}}{\partial x_k} + c_s\bar{\rho}\frac{k}{\epsilon}\tau_{kl}\frac{\partial \tau_{ij}}{\partial x_l}\right) \tag{11}$$

$$P_{ij} = -\bar{\rho}\tau_{ik}\frac{\partial \tilde{u}_j}{\partial x_k} - \bar{\rho}\tau_{jk}\frac{\partial \tilde{u}_i}{\partial x_k} \tag{12}$$

$$P^R_{ij} = -2\bar{\rho}\Omega_p\left(\epsilon_{jpk}\tau_{ki} + \epsilon_{ipk}\tau_{kj}\right) \tag{13}$$

$$\Phi^1_{ij} = -c_1\bar{\rho}\epsilon a_{ij} \tag{14}$$

$$\Phi^2_{ij} = -c_2\left(P_{ij} - \tfrac{1}{3}P_{kk}\delta_{ij} + \tfrac{1}{2}P^R_{ij}\right) \tag{15}$$

$$\begin{aligned}\Phi^w_{ij} &= c^w_1\frac{\bar{\rho}\epsilon}{k}\left(\tau_{kl}n_k n_l\delta_{ij} - \tfrac{3}{2}\tau_{ki}n_k n_j - \tfrac{3}{2}\tau_{kj}n_k n_i\right)f_w \\ &+ c^w_2(\Phi^2_{kl}n_k n_l\delta_{ij} - \tfrac{3}{2}\Phi^2_{ik}n_k n_j - \tfrac{3}{2}\Phi^2_{jk}n_k n_i)f_w\end{aligned} \tag{16}$$

The terms on the right-hand side of equation (10) are identified as diffusion, production by the mean flow, production caused by rotation, dissipation, slow redistribution, rapid redistribution and wall reflection. In this model, the local effects of flowfield anisotropy near wall are incorporated in the modeled term $\Phi^1_{ij} + \Phi^2_{ij} - 2/3\bar{\rho}\delta_{ij}$, contrary to other models which take into account the anisotropy of the dissipation tensor [22]. In these expressions, $k = \tau_{ii}/2$ is the turbulent kinetic energy, $a_{ij} = (\tau_{ij} - \frac{2}{3}k\delta_{ij})/k$ is the anisotropy tensor, c_1, c_2, c^w_1, c^w_2 are functions which depend on the second and third invariants $A_2 = a_{ij}a_{ji}$, $A_3 = a_{ij}a_{jk}a_{ki}$, the flatness coefficient parameter $A = 1 - \frac{9}{8}(A_2 - A_3)$ and the turbulent Reynolds number $R_t = k^2/\nu\epsilon$. The dissipation rate ϵ in

c_1	$1 + 2.58AA_2^{\frac{1}{4}}(1 - \exp(-(0.0067R_t)^2))$
c_2	$0.75A^{\frac{1}{2}}$
c_1^w	$-\frac{2}{3}c_1 + 1.67$
c_2^w	$\max(\frac{2}{3}c_2 - \frac{1}{6}, 0)/c_2$
f_w	$0.4k^{\frac{3}{2}}/\epsilon x_2$
ψ	$-c_{\epsilon 1}/8 < 1.5A\left(\frac{P_{ii}}{2\bar{\rho}\epsilon} - 1\right) < c_{\epsilon 1}/8$

Table 1: Functions used in the RSM model.

expression (10) is computed by means of the transport equation:

$$\frac{\partial}{\partial t}(\bar{\rho}\epsilon) + \frac{\partial}{\partial x_j}(\bar{\rho}\tilde{u}_j\epsilon) = J - (c_{\epsilon 1} + \psi)\bar{\rho}\frac{\epsilon}{k}\tau_{ij}\frac{\partial \tilde{u}_j}{\partial x_i} - c_{\epsilon 2}\bar{\rho}\frac{\tilde{\epsilon}\epsilon}{k} \tag{17}$$

where

$$J = \frac{\partial}{\partial x_i}\left(\bar{\mu}\frac{\partial \epsilon}{\partial x_i} + c_\epsilon \bar{\rho}\frac{k}{\epsilon}\tau_{ij}\frac{\partial \epsilon}{\partial x_j}\right) \tag{18}$$

and $\tilde{\epsilon} = \epsilon - 2\nu(\partial\sqrt{k}/\partial x_2)^2$. The diffusive terms are modeled by a gradient hypothesis:

$$\overline{\sigma_{ij}u_i''} - \frac{1}{2}\bar{\rho}\,\widetilde{u_k''u_k''u_j''} = (\bar{\mu}\delta_{jm} + c_s\bar{\rho}\frac{k}{\epsilon}\tau_{jm})\frac{\partial k}{\partial x_m} \tag{19}$$

The heat transfer of the turbulent flux is computed as:

$$\widetilde{h''u_i''} = -\frac{c_\mu k^2}{\epsilon}\frac{c_p}{P_{r_t}}\frac{\partial \bar{T}}{\partial x_i} \tag{20}$$

where c_p and P_{r_t} are the specific heat at constant pressure and the turbulent Prandtl number, respectively. The functions used in that model are listed in table 1. Values of the constant coefficients are $c_s = 0.22$, $c_{\epsilon 1} = 1.45$, $c_{\epsilon 2} = 1.9$, $c_\epsilon = 0.18$, $c_\mu = 0.09$. This model has already given good results in predicting rotating flows [18].

4 Numerical method

The finite volume technique is used to solve the full equations incorporating all the derivative terms. The numerical discretization scheme is second-order accurate in space and the time advancement uses a three-step Runge-Kutta method which is appropriate for simulating unsteady flows. A fixed pressure boundary condition is applied at the exit section of the channel. Boundary conditions for impermeable walls assume zero velocity and constant temperature, zero turbulent kinetic energy and the wall dissipation rate value $\epsilon_w = 2\nu(\partial\sqrt{k}/\partial x_2)^2$. For a permeable wall, a constant mass flow rate is imposed at the same temperature as the impermeable wall. Experimental measurements in the immediate vicinity of the permeable wall show that the velocity follows a Gaussian distribution.

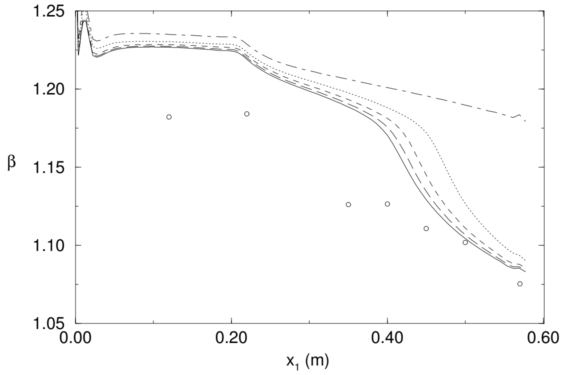

Figure 2: Axial variations of the coefficient β. $\circ$: experimental data. dot-dashed-line: $\sigma_s = 0.1$, dotted-line: $\sigma_s = 0.2$, dashed-line: $\sigma_s = 0.3$, long-dashed-line: $\sigma_s = 0.4$, solid-line: $\sigma_s = 0.5$

Investigations indicate also that the amplitude of the fluctuating velocity increases with increasing injection velocity [21]. From a physical point of view, the fluctuating part of the velocity is due to the injected fluid passing through the porous plate made of small bronze spheres and by the acoustics of the cavity. Based on these considerations, the boundary condition has been modeled by a twofold hypothesis. The first effect is taken into account by introducing a modeled turbulence level at the wall related to the mean injected velocity as $\sigma_s = (\widetilde{u_2''u_2''}/\tilde{u}_s^2)^{1/2}$. It is assumed that the material porosity is fine grained ($8\mu m$). The second effect which is not a turbulent effect is produced by a forcing with a Gaussian velocity distribution $P(u)$ in time but constant in space. The forcing is thus applied directly to the near wall mean velocity. Another point to emphasize concerns the pressure fluctuations of the flowfield. Considering that the permeable wall does not reflect the pressure fluctuations, the term Φ_{ij}^w of equation (16) is suppressed in the direction normal to the wall.

5 Numerical results

5.1 Steady flow regime

The objective is to reproduce the steady flow which evolves spatially from laminar to turbulent regimes. Due to the mass conservation equation, the flow Reynolds number $R_m = \rho_m u_m \delta/\mu$ based on the bulk density ρ_m and the bulk velocity u_m varies linearly with the axial distance along the channel so that it can be computed as $R_m = m x_1/\mu$. It ranges from zero to approximately 9 x 10^4. Numerical simulations are performed on refined meshes requiring 100 $\times$ 100, 200 $\times$ 200 and 200 $\times$ 300 nonuniform grids in x_1 and x_2 directions. For all the meshes, the grid in the normal direction x_2 is distributed using two geometric progressions from the wall to the center of the channel. For instance, the transverse resolution for the mesh 100 $\times$ 100 is 1 μm near the walls and 200 μm in the center of the channel. The dimensionless distance $x_2^+ = x_2 u_\tau/\nu$ between the first

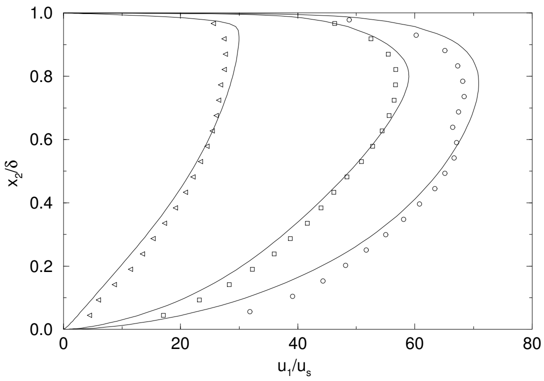

Figure 3: Mean dimensionless velocity profiles in different sections. $\sigma_s = 0.2$; Symbols: experimental data; solid line: RSM. 22 cm: $\triangleleft$; 45 cm: $\square$; 57 cm: $\circ$.

node and the wall is less than 0.3. In such conditions, this grid refinement provides full resolutions for the flow in the permeable wall region and for the boundary layer generated by the rigid walls. A grid-independence study was performed by checking the axial mean-velocity and the turbulence intensity. For the boundary condition of the fluid injection, different values of the coeffcient σ_s are considered. As a result, it is found that the effect of turbulence in injected fluid is to delay or to anticipate the transition process of the flow. This is illustrated in Figure (2) which shows, for different values of the injection paramater σ_s, the evolution of the integral momentum flux coefficient defined by :

$$\beta = \frac{\rho\delta \int_0^\delta \bar{\rho}\tilde{u}_1^2 dx_2}{\left(\int_0^\delta \bar{\rho}\tilde{u}_1 dx_2\right)^2} \tag{21}$$

The rapid drop of the coefficient β corresponds to the transition location. It can be noticed that the lower turbulence level $\sigma_s = 0.1$ is too small to trigger the transition process. This Figure reveals a qualitative agreement with the experimental data. Figure (3) shows the evolution of the dimensionless mean velocity profiles in different sections of the channel for the computation using $\sigma_s = 0.2$. The profile located in the section $x_1 = 22$ cm appears to be quite laminar whereas the profiles corresponding to the sections at 45 cm and 57 cm are found to be turbulent. The general shapes of the profiles display a good agreement with experimental data. Figures (4a), (4b) show, respectively, the streamwise and normal turbulent velocity fluctuations normalized by the bulk velocity $(\widetilde{u_1''u_1''})^{1/2}/u_m$, $(\widetilde{u_2''u_2''})^{1/2}/u_m$ in different sections. One can observe that the RSM model predicts fairly well the turbulence intensity which evolves from zero to approximately ten percent of the bulk velocity u_m. Note that previous computations of similar flow using a $k-\epsilon$ model have overpredicted the turbulence intensity by about 300 % in the post-transition zone [11, 12].

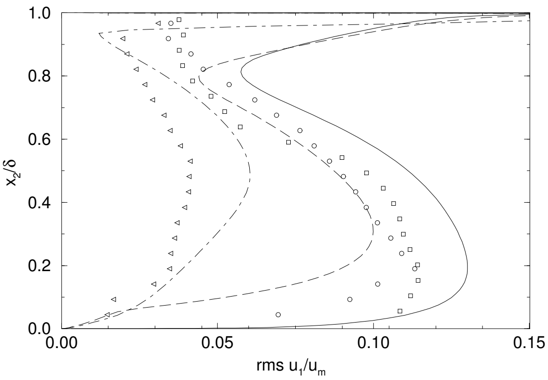

(a)

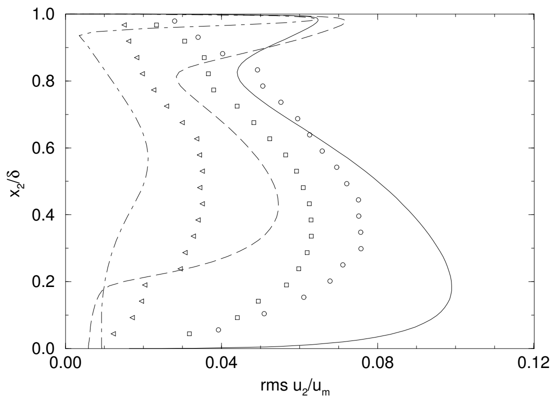

(b)

Figure 4: Turbulent velocity fluctuations normalized by the bulk velocity in different sections; (a)$(\widetilde{u_1''u_1''})^{1/2}/u_m$. (b)$(\widetilde{u_2''u_2''})^{1/2}/u_m$. $\sigma_s = 0.2$. $x_1 = 22$ cm: $\triangleleft$, dot-dashed line; 45 cm: $\square$, dashed line; 57 cm: $\circ$, solid line.

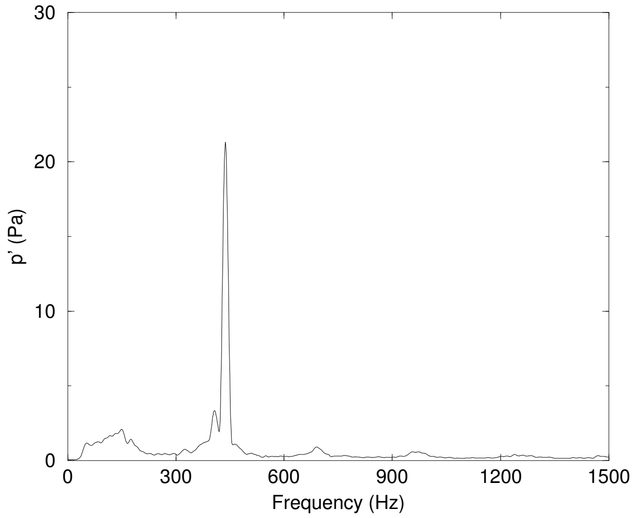

Figure 5: Experimental head end presssure spectrum

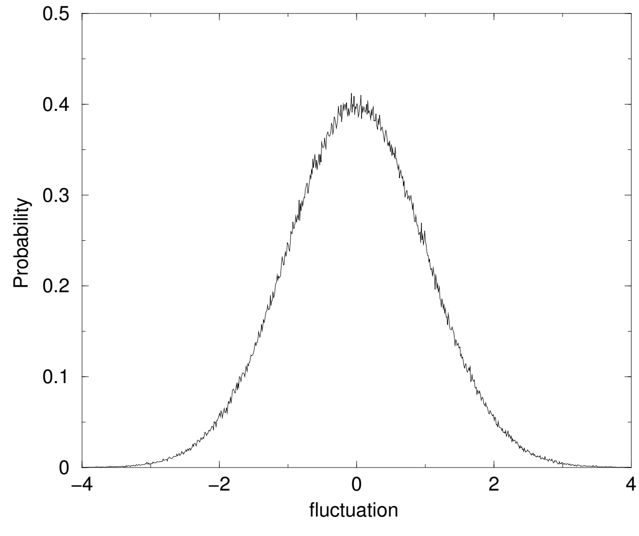

Figure 6: Gaussian probability for the fluctuating velocity.

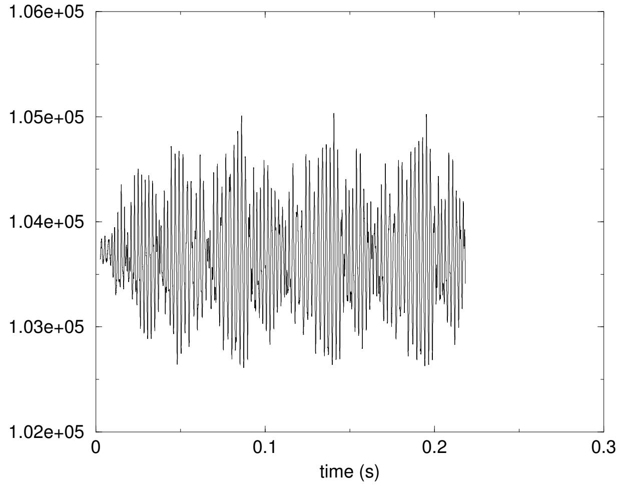

Figure 7: Head end pressure evolution versus time.

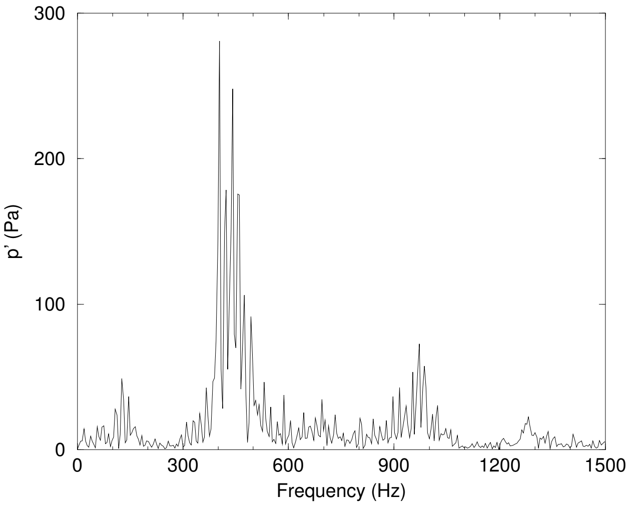

Figure 8: Head end pressure spectrum.

5.2 Unsteady flow regime

Several predictions of the oscillatory flowfield with natural instabilities are performed on meshes taking into account 600 $\times$ 100 and 600 $\times$ 200 non-uniform grids. The experiment has shown that this natural instability results in the development of near wall vortex structure. Thus, the grid is refined in the x_1 direction in order to reproduce accurately these flow vortices. For the computation, 2 $\times 10^6$ temporal iterations which represents 0.2 s of time are performed. The experimental pressure signal spectrum plotted in Figure (5) indicates that the flow presents a resonant regime at the frequency f = 407 Hz [21]. This is quite close to the frequency $f_1 = 3a_o/4L$ = 426 Hz which corresponds to the second longitudinal acoustic mode $3\lambda/4$ of the cavity. In this expression, the quantity a_o denotes the sound velocity. Indeed, visualisation tests [23] show the emission of flowfield vortices at this frequency. Therefore, the flow is characterized by an acoustic resonant regime. In general, the wavelength solutions of the Helmholtz equation are $\lambda_n = 4L/(2n+1)$ and the frequencies are $f_n = (2n+1)a_0/4L$. For the values $n = 0, 1, 2$, the first frequencies are 142, 426 and 711 Hz. It can be mentionned that the dimensionless resonant frequency is $\Omega^* = 2\pi\delta f_1/u_s = 30$ whereas the dimensionless critical frequency obtained by the linear stability analysis is $\Omega_c^* \approx 18.5$ [1]. In the computation, the Gaussian forcing has been artificially generated through fluctuating velocities $u_1' = \alpha\, \bar{u}_1\, P_1$, $u_2' = \alpha\, \bar{u}_2\, P_2$ where P_1 and P_2 are Gaussian distributions and the quantity α is a numerical coefficient. These distributions are obtained by $P_1 = t_1 \cos(2\pi t_2)$ and $P_2 = t_1 \sin(2\pi t_2)$, where $t_1 = \sqrt{-2\ln t_3}$, t_2 and t_3 are uniform random numbers in the interval [0,1] [24]. The distribution of the probability function P_1, (similary for P_2), is represented on Figure (6) for 10^6 events. In order to reproduce the level of the experimental noise, the coefficient α is assigned a value 0.02. As for the previous steady flow prediction, an injected turbulence intensity $\widetilde{u_2''u_2''}$ related to the porous material properties is also introduced at the wall. One result of interest is that the flow regime remains stable if no Gaussian forcing is imposed in the flowfield, regardless the intensity of the injected turbulence. Therefore, in order to trigger the instabilities, the Gaussian forcing has been applied and periodically refreshed in the immediate vicinity of the permeable wall. This technique was previously developed by Lupoglazoff and Vuillot for simulating this flow in laminar regime [25]. The present computed unsteady pressure signal is plotted on Figure (7). Figure (8) shows the head-end pressure spectrum that reveals the presence of the mode $3\lambda/4$. The fluctuating pressure peaks occur at 403 Hz and 422 Hz, with a resolution frequency of 5 Hz. The following modes $\lambda/4$, $7\lambda/4$ and $9\lambda/4$ are also observed on this Figure. Although the resonance frequency is well predicted, a discrepancy in the magnitude of the pressure fluctuations is observed between the experimental and computed signals in Figure (5) and Figure (8). This is due to the poral response or admittance which consists in adjusting the injected mass flow rate as a function of the local pressure [25]. However, in the present work, a zero poral response has been considered for the sake of simplicity which should explain the over-estimated level. Figures (9a), (9b), (9c) show the instantaneous vorticity contours $\bar{\omega}_i = \epsilon_{ijk}\partial\bar{u}_k/\partial x_j$ in the whole flow domain in the real scale at different time advancement $t = T_1/4$, $t = T_1/2$, $t = 3T_1/4$ where $T_1 = 1/f_1 = 0.00248$ s is the time period of the signal. The development of the acoustic boundary layer characterized by horizontal lines as well as the parietal vortex shedding of growing size which results from natural instabilities are well observed in the channel. The structures are visible in the final part of the channel and move toward the open exit. It can be seen that the intensity of the vortices increases with the downstream distance. Figures (9d) (9e) (9f) show the enlarged view of the instantaneous

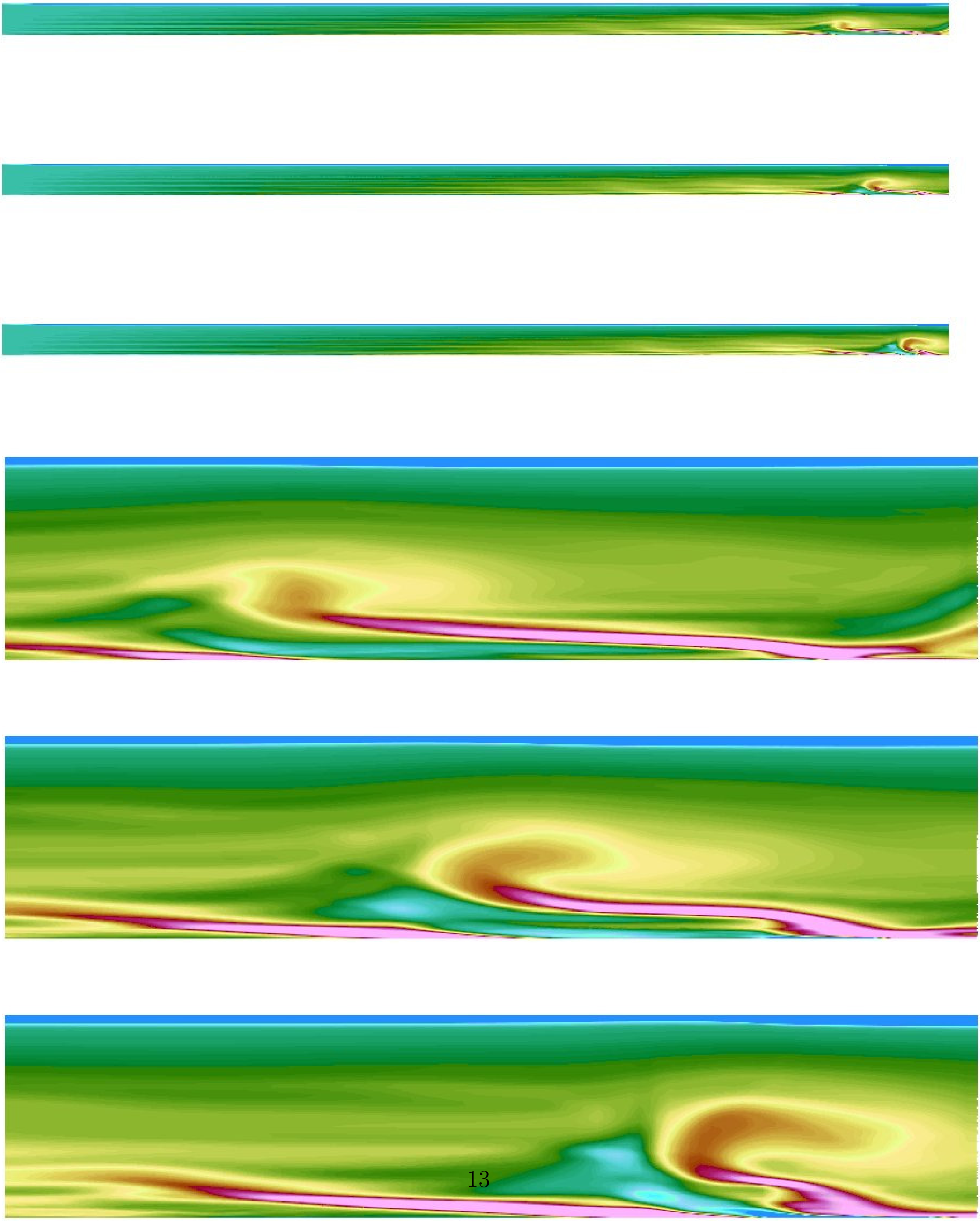

(a)

(b)

(c)

(d)

(e)

(f)

Figure 9: Instantaneous vorticity contours at different times: $t = T_1/4$, $t = T_1/2$, $t = 3T_1/4$. (a),(b),(c): animation of real aspect ratio view; (d),(e),(f): animation of enlarged view.

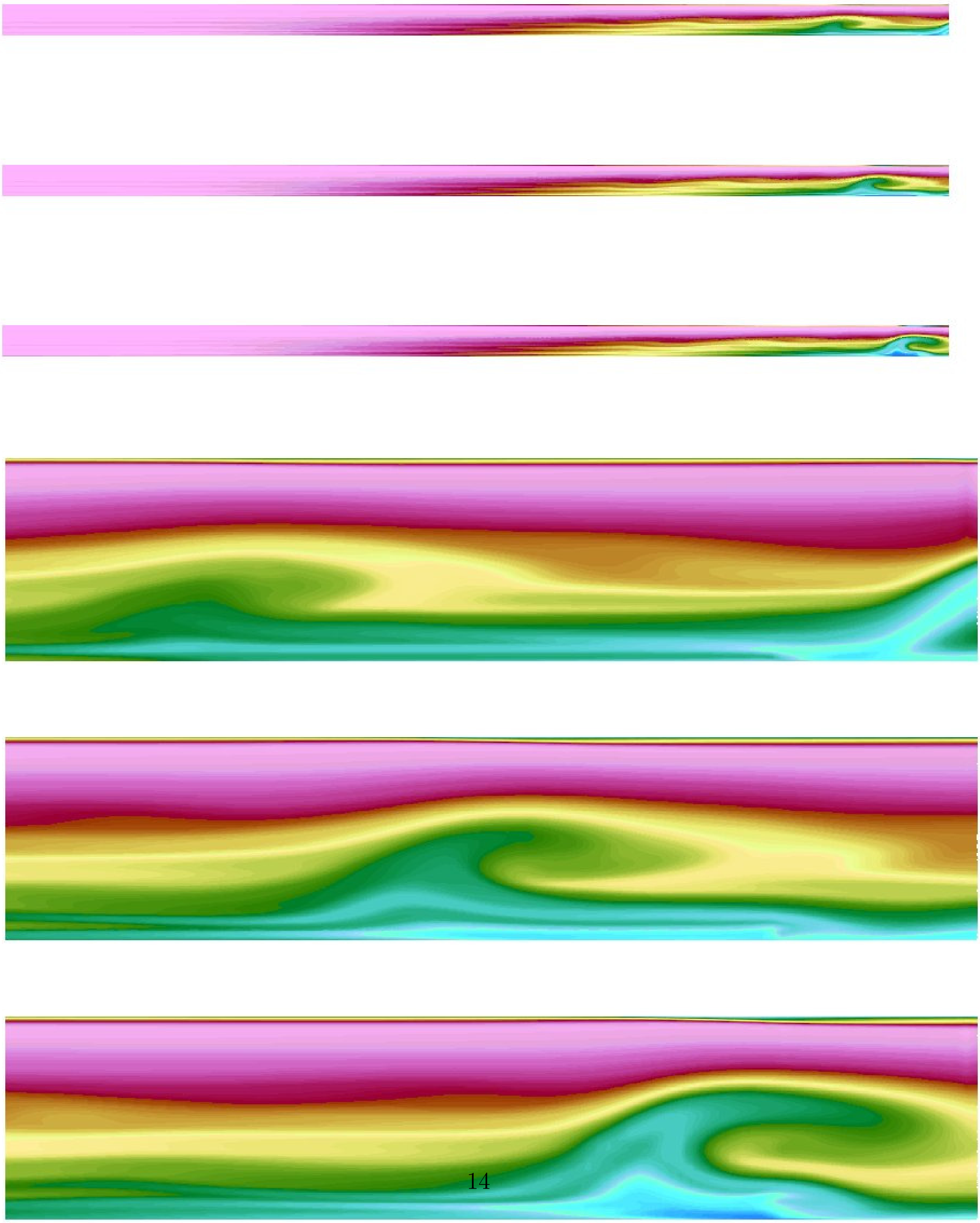

(a)

(b)

(c)

(d)

(e)

(f)

Figure 10: Instantaneous entropy contours at different times: $t = T_1/4$, $t = T_1/2$, $t = 3T_1/4$. (a),(b),(c): animation of real aspect ratio view; (d),(e),(f): animation of enlarged view.

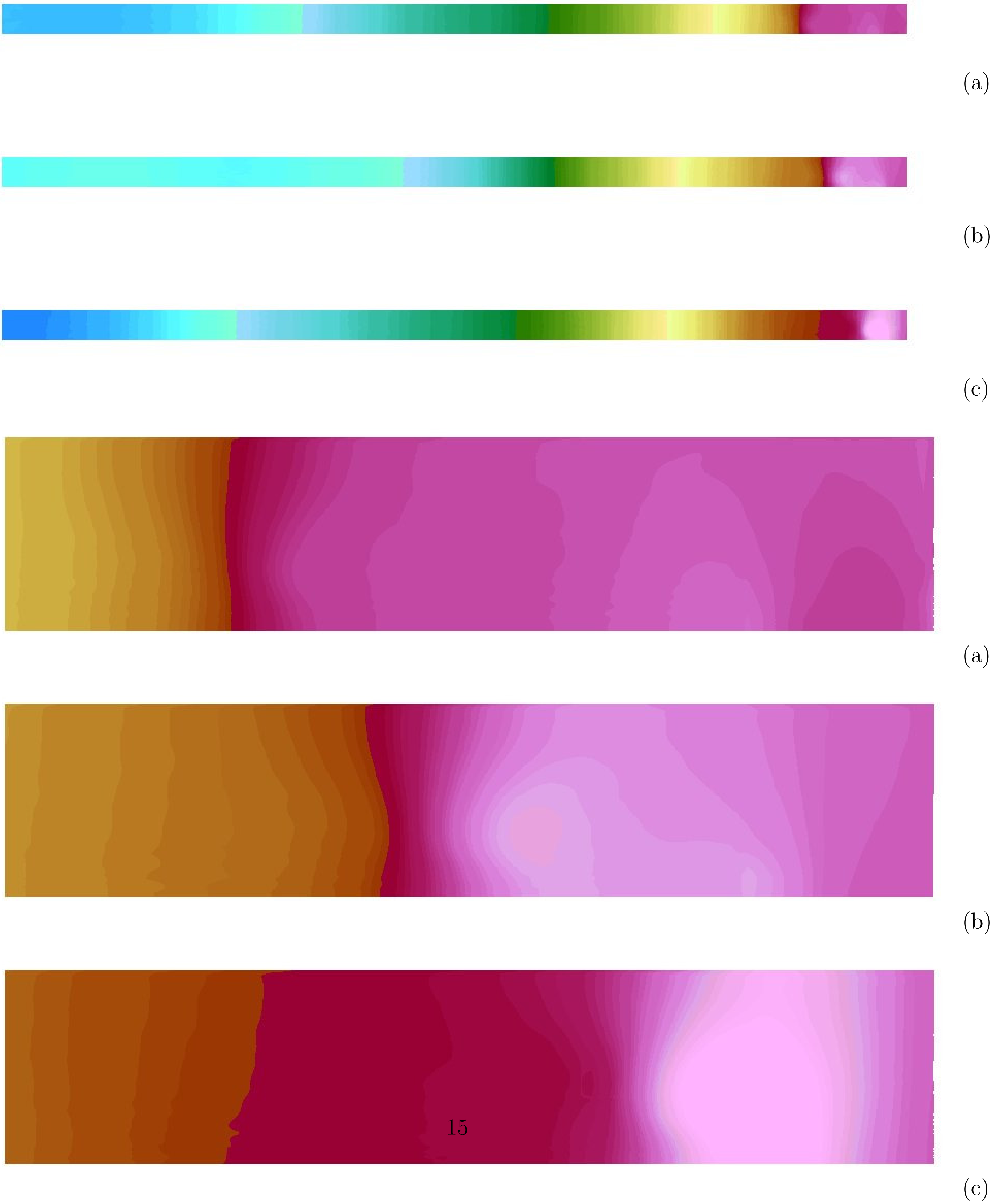

Figure 11: Instantaneous pressure contours at different times: $t = T_1/4$, $t = T_1/2$, $t = 3T_1/4$. (a),(b),(c): animation of real aspect ratio view; (d),(e),(f): animation of enlarged view.

Figure 12: Enlarged view of the turbulent Reynolds number contours $R_t = k^2/\nu\epsilon$. $0 < R_t < 1620$.

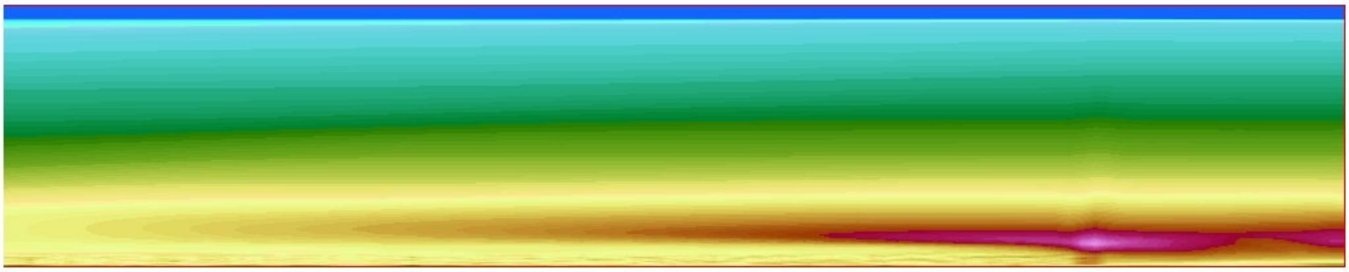

Figure 13: Enlarged view of the instantaneous vorticity contours for the $k - \epsilon$ model.

vorticity contours near the exit of the channel and reveal the flow structures. It is of interest to note that these structures are quite similar to those obtained by experimental imaging technique using Acetone Planar Laser-Induceed Fluorescence (PLIF) [23]. Note that LES technique has also produced similar structures for a flow inside a plane channel included inclined backward-facing traling edge with a simplifed nozzle [26]. The evolution of the mean vorticity can be explained by its transport equation (22) in unsteady flow regime :

$$\frac{\partial \tilde{\omega}_i}{\partial t} + \tilde{u}_j \frac{\partial \tilde{\omega}_i}{\partial x_j} = \nu \frac{\partial^2 \tilde{\omega}_i}{\partial x_j \partial x_j} - \frac{\partial}{\partial x_j} \left(\overline{\omega_i'' u_j''} \right) + \tilde{\omega}_j \tilde{S}_{ij} + \overline{\omega_j'' S_{ij}''} + O \tag{22}$$

where O represents the term of compressible flow effects which can be neglected in the present case due to the low Mach number value which is lower than 0.25. For a two-dimensional computation, the mean vorticity is along the spanwise direction $\tilde{\omega}_3 = (\partial \tilde{u}_2/\partial x_1 - \partial \tilde{u}_1/\partial x_2)$. It is created by the interaction between the flow injected in the normal direction to the permeable wall and the flow coming from the head end of the channel in the streamwise direction. The vorticity is convected by the main flow velocity and modified by the laminar and turbulent diffusion processes as indicated by equation (22). The gain or loss of the mean vorticity is influenced by the correlation term $\overline{\omega_j'' S_{ij}''}$ composed of the fluctuating vorticity components and by fluctuating strain rates. The vortex-stretching contribution $\tilde{\omega}_j \tilde{S}_{ij}$ is reduced to zero for two-dimensional mean flow. The convection velocity of the vortex has been computed by considering the passage of the vortex through some cross sections of the channel at different time advancements. It is of interest to note that the ratio of the convection velocity to the bulk velocity in the channel takes the approximate value 0.76. Note that the bulk velocity has been considered in that case because the local flow velocity presents too high variations versus the channel height as previously observed in Figure (3) although it relates the previous computation for the steady flow. This result regarding the different velocity for the fluid and the vortex corresponds to usual case of flow physics. Figures (10a) (10b) (10c) describe the instantaneous entropy contours in the whole flow domain and illustrates the instabilities of the boundary layers near the permeable wall. Figures (10d) (10e) (10f) show the enlarged view of the entropy contours and describe the instantaneous coherent eddies of the flowfield. Figures (11a) (11b) (11c) show the pressure contours of the whole flow domain. These figures reveal that the pressure is almost uniform in each cross section of the channel. Enlarged view of the pressure contours are observed on Figures (11d) (11e) (11f). It is verified that the passage of the vortices locally tends to decrease the static pressure. Figure (12) shows the contours of the turbulent Reynolds number and reveals that the turbulence is mostly developed near the impermeable wall in comparison with the permeable wall region. The turbulent Reynolds number $R_t = k^2/\nu\epsilon$ ranges from zero to the approximate value 1600. Other numerical flows predictions have been computed using first order turbulence model such as $k - \epsilon$ with a low Reynolds number formulation for appoaching walls [27]. For the same boundary conditions than for the RSM computation, one can notice that the $k - \epsilon$ model is not able to reproduce the large flow structures, as indicated in Figure (13) which shows enlarged view of the instantaneous vorticity contours [28]. Explanation of that results should be attributed to the dissipative behavior of the scalar turbulent eddy viscosity in the $k - \epsilon$ model which has the effect of smoothing the instabilities. In the present case, it has been demonstrated that second order turbulence model has better properties than first order turbulence model.

6 Conclusion

An advanced second-order turbulence model has been used to compute flows with complex physics, such as strong effects of the streamlines curvature caused by the fluid injection, different flow regimes from laminar to turbulent, transition, unsteady flow involving an acoustic resonance. Both steady and unsteady flows are fairly well predicted numerically by RSM model in good agreement with the experiments. For the steady flow, it has been found that the Reynolds stress model is able to reproduce the mean velocity profile, the transition process and the turbulent stresses. For the unsteady flow, it has been demonstrated that the RSM turbulence model is able to generate the vortex shedding mechanism which results from natural instabilities. The coherent structures of the computed flow have been visually observed in agreement with experimental flow visualizations. Other computations show that first order turbulence model such the $k-\epsilon$ is not suited for predicting both steady and unsteady flows in SRM.

References

[1] G. Casalis, G. Avalon, and J P. Pineau. Spatial instability of planar channel flow with fluid injection through porous walls. *Physics of Fluid*, 10(10):2558–2568, 1998.

[2] R. Dunlap, A. M. Blackner, R. C. Waugh, R. S. Brown, P. G., and Willoughby. Flow field studies in a simulated cylindrical port rocket chamber. *Journal of Propulsion and Power*, 6(6):690–704, 1990.

[3] G. A. Flandro. Vortex driving mechanism in oscillatory rocket flows. *Journal of Propulsion and Power*, 2(3):206–214, 1986.

[4] K. W. Doston, S. Koshigoes, and K. K. Pace. Vortex shedding in a large solid rocket motor without inhibitors at the segment interfaces. *Journal of Propulsion and Power*, 13(2):197–206, 1997.

[5] P. Venugopal, F. M. Najjar, and R. D. Moser. DNS and LES computations of model solid rocket motors. AIAA Paper 2000–3511, July 2000. In 36th AIAA/ASME/SAE/ASEE Joint Propulsion Conference and Exhibit.

[6] J. Silvestrini. *Simulations des grandes échelles des zones de mélange; Application à la propulsion solide des lanceurs spatiaux.* PhD thesis, Institut National Polytechnique de Grenoble, 1996.

[7] M. Lesieur and O. Metais. New trends in large-eddy simulations of turbulence. *Ann. Rev Journal of Fluid Mechanics*, 28:45–82, 1996.

[8] F. Vuillot. Vortex-sheeding phenomena in solid rocket motor. *Journal of Propulsion and Power*, 11(4):626–639, 1995.

[9] S. Apte and V. Yang. Unsteady flow evolution in porous chamber with surface mass injection, part 1 : Free oscillation. *AIAA Journal*, 39(8):1577–1586, 2001.

[10] A. A. Sviridenkov and V. I. Yagodkin. Flows in the initial sections of channels with permeable walls. *Fluid Dynamics*, 11:43–48, 1976.

[11] J. S. Sabnis, R. K. Madabhushi, and H. McDonald. Navier-Stokes analysis of propellant rocket motor internal flows. *AIAA Journal*, 5(6):657–664, 1989.

[12] B. Chaouat. Computation using $k-\epsilon$ model with turbulent mass transfer in the wall region. 11^{th} *Symposium on Turbulence Shear Flows*, 2:2.71–2.76, 1997.

[13] C. G. Speziale, S. Sarkar, and T. B. Gatski. Modelling the pressure-strain correlation of turbulence: an invariant dynamical systems approach. *Journal of Fluid Mechanics*, 227:245–272, 1991.

[14] R. Schiestel. Multiple-time scale modeling of turbulent flows in one point closures. *Physics of Fluid*, 30(3):722–731, 1986.

[15] R. A. Beddini. Injection-induced flows in porous-walled ducts. *AIAA Journal*, 11(6):1766–1773, 1986.

[16] R. Dunlap, P G. Willoughby, and R W. Hermsen. Flowfield in the combustion chamber of a solid propellant rocket motor. *AIAA Journal*, 12(10):1440–1443, 1974.

[17] B. E. Launder and N. Shima. Second moment closure for the near wall sublayer: Development and application. *AIAA Journal*, 27(10):1319–1325, 1989.

[18] B. Chaouat. Simulations of channel flows with effects of spanwise rotation or wall injection using a Reynolds stress model. *Journal of Fluid Engineering, ASME*, 123:2–10, 2001.

[19] B. Chaouat. Numerical predictions of channel flows with fluid injection using Reynolds stress model. *Journal of Propulsion and Power*, 18(2):295–303, 2002.

[20] E. Lamballais, O. Métais, and M. Lesieur. Spectral-dynamic model for large-eddy simulations of turbulent rotating flow. *Theoret. Comput. Fluid Dynamics*, 12:149–177, 1998.

[21] G. Avalon, G. Casalis, and J. Griffond. Flow instabilities and acoustic resonance of channels with wall injection. AIAA Paper 98–3218, July 1998. In 34th AIAA/ASME/SAE/ASEE Joint Propulsion Conference and Exhibit.

[22] K. Hanjalic, I. Hadzic, and S. Jakirlic. Modeling turbulent wall flows subjected to strong pressure variations. *Journal of Fluid Engineering, ASME*, 121:57–64, 1999.

[23] G. Avalon, B. Ugurtas, F. Grish, and A. Besson. Numerical computations and visualization tests of the flows inside a cold gas simulation with characterization of a parietal vortex shedding. AIAA Paper 2000–3387, July 2000. In 36th AIAA/ASME/SAE/ASEE Joint Propulsion Conference and Exhibit.

[24] D. E. Knuth. *The Art of Computer Programming.* Addison-Wesley Publishing Compagny, 1998.

[25] N. Lupoglazoff and F. Vuillot. Numerical simulations of parietal vortex-shedding phenomenon in a cold flow set-up. AIAA Paper 98–3220, July 1998. In 34th AIAA/ASME/SAE/ASEE Joint Propulsion Conference and Exhibit.

[26] P. Comte, J. H. Silvestrini, and P. Begou. Streamwise vortices in larges-eddy simulations of mixing layers. *Eur. J. Mech. B/Fluids*, 17(4):615–637, 1998.

[27] H. Myong and N. Kasagi. A new approach to the improvement of $k - \epsilon$ turbulence model for wall-bounded shear flows. *JSME International Journal*, 33(1):63–72, 1990.

[28] B. Chaouat and R. Schiestel. Prévision d'écoulements instationnaires de canal soumis à une injection pariétale par un modèle RSM. Technical report, ONERA, 2001. RTS 4/6174.